

Design and Control Concepts of a Hyper Redundant Haptic Interface for Interaction with Virtual Environments

Marc Ueberle, Nico Mock
Control Systems Group, Faculty IV - EECS
Technische Universität Berlin
D-10587 Berlin, Germany
ueberle@rs.tu-berlin.de
mock@rs.tu-berlin.de

Angelika Peer, Christian Michas, Martin Buss
Institute of Automatic Control Engineering
Technische Universität München
D-80290 München, Germany
angelika.peer@ei.tum.de
christian.michas@tuev-sued.de
martin.buss@ei.tum.de

Abstract—This paper discusses the design concept of a hyper-redundant haptic interface with 10 actuated degrees-of-freedom (DOF). The kinematical redundancies allow a significantly larger workspace, while reducing the overall device size. Moreover, an increase in a variety of dexterity measures and a singularity robust redundancy resolution can be achieved. Numerical studies comparing the performance of local redundancy optimisation techniques are presented. Besides a construction possibility for virtual environments based on methods for visual and haptic rendering is presented.

I. INTRODUCTION

Haptic interfaces are force feedback devices enabling bidirectional human system interactions via the sense of touch. Being able to exert and react to the operator's motions and interaction forces they are used to mimic the dynamic behaviour of virtual or remote environments in virtual reality and telepresence systems. Although in recent years haptic devices have been successfully implemented in various task domains including e. g. medical and surgical VR systems [1], rehabilitation, tele- and micromanipulation [2], telemaintenance, virtual prototyping, scientific visualisation [3], and education [4], their enormous application potential does not seem to be exhaustively investigated and exploited.

The exploration of novel applications is often impaired by the unavailability of qualified haptic hardware. Scenarios involving operations in large regions are e. g. little studied mostly due to the fact that commercially available haptic devices suffer from comparatively small workspaces. Among the reasons for this is the design rationale of most interfaces to provide low dynamic properties. A large workspace seems to be contrary to this requirement because it usually leads to large and heavy interfaces with reduced mechanical stiffness. A possible solution to this problem is the introduction of actuated kinematic redundancies. These can be exploited for the avoidance of interior singularities allowing for significantly larger workspaces without increase of the device size. Besides the increase of workspace the redundant kinematical DOF offer a potential for operator collision avoidance and improvement of the dynamic properties and output capability. Even though redundancies have been successfully introduced in industrial robot designs, see e.g. [5], this concept is only little

explored and employed for haptic interface kinematics. The only kinematically redundant haptic devices known to the authors are exoskeleton constructions, off-the-shelf redundant industrial robots, and the 7 DOF DLR light-weight robots [6] which are, however, not specifically designed for haptic applications.

In order to offer a haptic device allowing high force tasks in large volumes we designed the hyper-redundant system VISHARD10 (Virtual Scenario Haptic Rendering Device with 10 actuated DOF). This design is based on the experiences obtained from a non-redundant haptic device VISHARD6 previously developed [7]. Both devices employ a force-torque sensor for active force feedback control to shape the device dynamics. Directed towards versatility and extensibility the objective is to provide a testbed and experimental environment for a rapid evaluation of haptic applications.

This paper is organised as follows. Section II briefly reviews the requirements and state of the art of haptic hardware also discussing the use of kinematic redundancies. Section III presents the system design of VISHARD10 and section IV basic control strategies along with the inverse kinematics solution techniques. Section V presents a construction possibility for virtual environments based on methods for visual and haptic rendering. Finally numerical studies evaluating the performance of local redundancy optimisation techniques are presented in section VI.

II. KINESTHETIC DEVICE DESIGN

A. Requirements

An 'ideal' haptic device provides for a large variety of haptic applications a completely transparent interface to the remote or virtual environment, i. e. the user cannot detect any difference to the interaction with real objects. The transparency and versatility of haptic devices is affected by a number of design criteria characterising its performance.

- *Dynamic properties:* In unconstrained motion (e.g. free space simulations) no force generated by the natural device dynamics should be felt by the operator. Accordingly, the mechanical device impedance, i. e. the inertia, mass, and friction, should be minimised. An additional significant lowering of the dynamic

properties can be achieved by active force feedback and/or acceleration control.

- *Stiffness*: The maximum stiffness of virtual walls a haptic device is able to render is dependent on the mechanical rigidity and the stiffness of the achievable stable control. The control stiffness is enhanced by an increase of the mechanical damping (friction), the sampling rate, and the resolution of the sensors and actuators [8]. The mechanical rigidity also affects the device frequency response. The flexibility of the mechanical structure may result in non-collocated flexible modes degrading the device closed-loop bandwidth and active force control performance if not compensated by dedicated control laws, see e.g. [9]. To realise an accurate positioning as well as a wide output bandwidth the backlash of the joint components has to be low.
- *Output capability*: The device output capability by means of maximum force, velocity, and acceleration defines limits for the haptic interactions that can be rendered. It was for instance found that the ability to display impulsive forces e.g. from impacts and hard contacts is strongly related to the deceleration capability [10]. Moreover, a low output capability can reduce the performance of active force feedback control because actuation saturation may reduce the closed loop robustness.
- *Workspace*: The decision for the number of the DOF and the size of the workspace mainly affects the range and variety of applications the interface can be applied for.
- *Extensibility*: Besides the workspace and the output capability the most influential factor for the versatility of the device is its extensibility. The addition of complex end-effectors requires sufficient mounting space and torque capability to compensate for the payload.
- *Safety*: If the application calls for a large interface with high output capability careful attention has to be paid to safety measures ensuring that a computer or device malfunction does not result in user injury. A common and comparatively reliable procedure is to cut off the motor power in case joint velocities go beyond a given threshold which usually happens when the system becomes unstable. However, offering a limitation of the kinetic energy this method also degrades the dynamic performance.

It is intuitively clear that these requirements are contrary and one has to balance amongst them Human perceptual thresholds can be used to establish general design guidelines [11], but hardware limitations usually necessitate the definition of task specific requirements.

B. State of the art

Nowadays, kinesthetic haptic interfaces are commercially available for a wide range of application areas. In order to provide maximum performance a variety of highly specialized devices has been developed. This includes for

instance the "Rutgers ankle" orthopedic rehabilitation interface [12] or the Laparoscopic Impulse Engine (Immersion) with a kinematical design and output capability matching exactly the requirements of minimally invasive surgical simulation.

For general tool based applications the PHANToM devices (SensAble Technologies) developed at MIT [13] are the most widely used. They are available in a variety of sizes and 3 or 6 actuated DOF. Offering low dynamic properties they are able to render free-space in a high-quality. The haptic display of stiffness is, however, limited due to the low physical damping present in the joints. Another passive design with disturbance forces very close to the human perceptual threshold is the Freedom 6S (MPB Technologies), the commercial version of Freedom 7, see [14]. As a result of their wide frequency response they are capable of displaying tactile information by providing high frequency vibrations. These vibrotactile stimuli allow haptic exploration of virtual objects by using a tool. However, a realistic direct interaction with the user's finger or hand cannot be realised; for instance the human discrimination of small scale shapes requires distributed tactile stimuli.

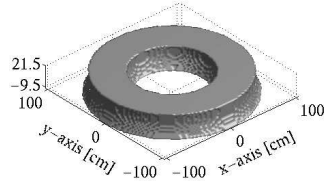
Another deficiency of these interfaces is the lack of force measurement. As a consequence they cannot be used for applications that fundamentally require the device to render an admittance. An example for such an application is a bone drilling training scenario where the surgeon should learn to apply a dedicated constant force to the drill [15]. Commercial devices providing force sensing are the DELTA Haptic Device (FORCE dimension) [16] and the VIRTUOSE 6D (Haption). Both provide force feedback in six DOF with increased (but still moderate) force capability compared to the PHANToM 1.5/6 DOF device.

A common deficiency of these commercially available haptic devices is their comparatively small workspace and low force capability forbidding e.g. large ergonomic studies and the display of stiff immovable walls during assembly and disassembly simulations. One of the reasons is that the design rationale to have low dynamic properties is contrary to other requirements as versatility or large workspace.

For haptic realisation of tasks requiring a large workspace and high force capability often off-the-shelf industrial robots are used [17], [18]. These robots are, however, not optimised for interactions with humans; the force capability exceeds by far the strength of a human and the mechanical stiffness is much larger than required for haptic applications. Consequently, these devices show major deficiencies regarding dynamic properties and safety aspects. Interfaces with human matched force capability and workspace, i.e. devices filling the gap between passive designs and industrial robots, are uncommon and rarely available. Two of the very few examples are the Excalibur device [19] with very high peak stiffness and the *HapticMASTER* (FCS Control Systems) [20] showing good performance regarding deceleration capability. Both provide 100 N continuous force in 3 DOF but in a rather limited workspace.



Fig. 1. Workspace of VISHARD6



Another approach to provide a large workspace combined with high force are exoskeleton constructions with jointed linkages fixed to the operator. A drawback of arm exoskeletons is that they tend to be quite complex and encumbering as for instance the SARCOS dexterous master. The fact that exoskeletons are firmly attached to the user causes comfort and safety problems.

C. Kinematic redundancies

One of the reasons for the limited workspace of most haptic devices is based on the kinematical design which is almost exclusively non-redundant (equal number of actuated joints and DOF at the end-effector). Large areas of the workspace are often not available for haptic simulations due to the existence of interior singularities. Singularities are positions in space where the robot loses a DOF. Whereas in common industrial robot applications it is frequently allowed to drive the robot through such singularities it is necessary to circumvent these locations in haptic systems for the following reason: around these positions the dynamic properties of the robot degrade due to the fact that high joint velocities only produce small endeffector velocities in certain directions. This results in a significant impairment of the end effector output capability regarding acceleration and velocity. Because the device can be moved by the human operator at will motions along these directions cannot be avoided by trajectory planning methods.

To illustrate the effect of interior singularities the workspace of VISHARD6, a 6 DOF haptic interface [7], can be viewed. Fig. 1 shows the singularity free translational working volume allowing arbitrary orientations of the end-effector in the range of 360° , 90° , and 360° for the angle of roll, pitch, and yaw, respectively. Although the working area is comparatively large an area in the center of the workspace is not available for haptic interaction due to interior singularities. Singularities are also the reason for the limitation of the angular workspace. It is in general true that an angular workspace of 360° around each axis is not achievable for non-redundant 6 DOF robots.

These fundamental limitations of non-redundant manipulators are the motivation for the design of a haptic interface with actuated kinematical redundancies. These systems allow for a change of the internal configuration without changing the position and orientation of the end-effector. This kind of motion is called *null-space movement* or *selfmotion*. A well directed control of the selfmotion may contribute to increase the overall system performance.

The following summarises some of the well known attractive features available in redundant kinematical designs.

- *Workspace*: The redundant DOF can be used to avoid interior singularities. This can drastically increase the workspace while simultaneously reducing the device size.
- *Dynamic properties*: The selfmotion can be controlled to maximise inertial performance criteria and to reduce friction forces at the end-effector.
- *Output capability*: Also feasible is the maximisation of performance criteria affecting the output capability as e.g. force/velocity transmission or acceleration capability.
- *Collision avoidance*: Redundancies offer an increased potential for collision avoidance with the environment and human operator.

Although these attractive features kinematical redundancies are rarely used for haptic devices. A possible explanation is the increased cost and complexity of the mechanical design. To control the redundant DOF a computational augmentation is unavoidable. Also, the introduction of additional joints seems to be contrary to the objective of low inertia and high stiffness. The potential reduction of the device size relaxes these disadvantages. Moreover, the removal of the interior singularities allows to operate in workspace regions with increased stiffness and output capability.

III. DESIGN OF VISHARD10

A. Design rationale

The main design objective for the new hyper-redundant haptic interface is to provide a versatile haptic display with distinct advantages compared to existing solutions with respect to applicability for a variety of applications; large workspace free of singularities; high payload to accommodate various application specific end-effectors as e.g. surgical tools like drills [1] or scissors, to mount tactile stimulation actuators for combined kinesthetic and tactile feedback; offer redundancy to avoid user interference; provide dual-arm haptic interaction with full 6 DOF capability (again redundancy facilitates collision avoidance between the two arms).

This versatility is advantageous as it provides a benchmarking testbed for the development and feasibility studies of novel haptic applications. When new applications are developed, which require a certain workspace or force capability, the proposed redundant device can be constrained to these specifications by appropriate controller design; this includes the development of dedicated inverse kinematics algorithms incorporating the specific needs of these applications. Once the new haptic application has been rudimentarily developed using VISHARD10 and the feasibility is verified, a tailored, highly specialised haptic display can be developed.

Subsequent investigations will have to tackle novel redundancy exploitation techniques specific to the goal of haptic human-device interaction and therefore very different from the known redundancy control methods in the

literature. Main difference is that the trajectories are not known in advance as the device can be moved by the human operator at will. Furthermore, the human comfort has to be considered. We expect for instance that the device selfmotion has to be simple to understand and anticipated by the operator. Unpredictable motions are likely to discomfit the user by creating the feeling to interact with an unpredictable piece of hardware.

B. Standard 7 DOF anthropomorphic arm designs

Our first considerations regarding the kinematic design of a redundant interface have been focused on the class of standard kinematical designs consisting of a 3-jointed spherical shoulder, a single elbow joint, and a 3-jointed spherical wrist. These arms can be described as anthropomorphic after [21]. Exemplarily, a configuration with a wrist in roll-pitch-roll configuration is illustrated in figure 2. The strength of these mechanisms is the size of the workspace which is optimum for 7 DOF robots in terms of the ratio of the arm length to the working volume. The translational workspace is a sphere with an interior singularity at the center. The angular workspace is 360° around each axis since singularities in the wrist can be avoided by rotating the elbow around the line from the shoulder to the wrist. A kinematic analysis of the design shown in figure 2 is presented in [22]. Among the drawbacks we identified for 7 DOF anthropomorphic arms are:

- *Gravitational load:* Only the first joint axis is designed to be vertical for arbitrary positions and orientations of the end-effector. As a consequence high motor torque is required to compensate for gravitational load.
- *Interior singularity:* The singularity in the center of the workspace impairs the dexterity and thus the performance of the device when moving the end effector close to the shoulder. An elimination of this singularity requires at least two additional redundant joints placed between the shoulder and the wrist.
- *Safety:* The most critical deficiency is the selfmotion of anthropomorphic 7 DOF arms, the rotation of the upper and forearm. Especially in case of operating with the end-effector close to the shoulder the elbow-orbit may deeply intrude into the operator's workspace bearing the risk for severe conflicts between the elbow joint and the user. The safety aspect can be solved by using a 4-jointed roll-yaw-pitch-roll wrist as described in [23]. Then the position of the elbow can be controlled to prevent collisions with the operator as singular wrist configurations can be avoided with the selfmotion of the redundant wrist. This 8 DOF solution, however, intensifies the deficiency regarding gravitational load significantly.

C. Haptic device description

In order to circumvent these deficiencies of anthropomorphic arms we finally decided for a mechanism without a 3-jointed spherical shoulder. The kinematic structure of

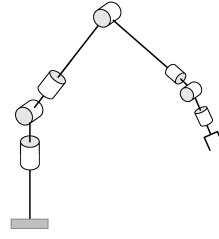


Fig. 2. Typical 7 DOF anthropomorphic robot arm

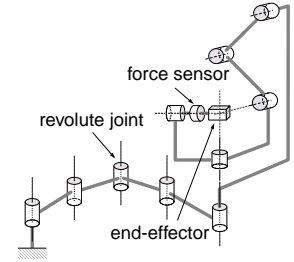


Fig. 3. Hyper-redundant haptic device VISHARD10

the hyper-redundant design with 10 DOF, VISHARD10, is depicted in Fig. 4, the link length design is summarised in Tab. I. It shows the reference configuration with all joint angles θ_i defined to be zero. In Fig. 5 the prototype is shown in a typical operational configuration.

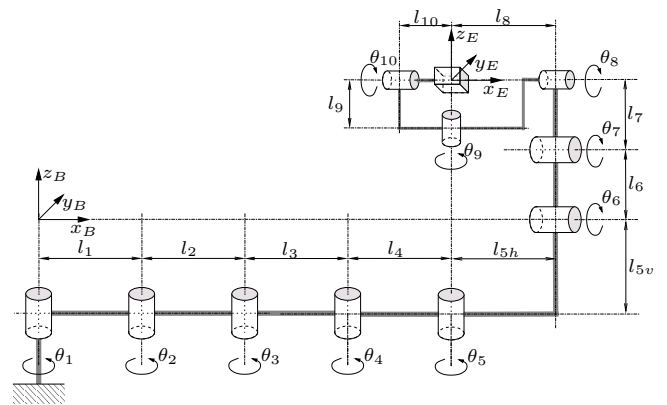


Fig. 4. Kinematical model of VISHARD10

The first five joints are arranged in a SCARA configuration with vertical axes avoiding the need for an active compensation of gravity. This segment is assigned for the positioning of the end effector in the x - y -plane. Although a SCARA segment with three links is sufficient for the elimination of the singularity in the center of the planar workspace we decided for an arm with 4 revolute joints (4R) for two reasons: First, it is well known that the 4R arm provides improved dexterity compared to the 3R arm [24] and second, the avoidance of user interference is much simpler to achieve.

Alternatively we weighed up the use of a 2 DOF linear axes design for the positioning in the x - y -plane as this also provides an interior singularity free workspace. This mechanism, however, suffers from a significantly reduced workspace; two prismatic joints with a length of one meter each are required to achieve a workspace of $1 \times 1 \text{ m}^2$ whereas an 4R arm with a total length of two meters can provide a sphere with radius 2 m. Moreover, as the base of the 4R arm is less bulky it is better suited for two arm simulators with two haptic devices.

Joints 6 and 7 are assigned to adjust the height of the end-effector. One simple inverse kinematics solution for them is the imitation of a prismatic joint by means of not changing the end-effector position in the x - y -plane.



Fig. 5. Bimanual haptic display ViSHARD10

The decision for two revolute joints over one prismatic joint is amongst other things due to the fact that off-the-shelf prismatic joints matching our requirements regarding velocity, mass, stiffness, velocity, and zero backlash could not be found on the market and modularity of the rotational joint components is kept.

Joint 5 is used to prevent singular configurations in the wrist formed by joints 8, 9, 10. Despite tending to an increased wrist size we decided for a yaw instead of roll orientation for joint 8 to obtain decoupling of the wrist configuration from the end-effector height. This mechanism has a singularity when the axes of joint 8 and 10 have the same orientation which has to be avoided by a rotation of joint 5. An inverse kinematics algorithm for a similar kinematic design providing bounded and well-conditioned joint rates for arbitrary angular velocities of the end-effector has been presented in [25].

The axes of joint 5, 8, 9, 10 intersect at one point which is located 5 cm in front of the force-torque sensor (assuming that the motion of joint 6 and 7 is controlled accordingly). This enables the operator to grip the end-effector at the point where the angular DOF are mechanically decoupled from the translational ones as for example desired for simulations involving direct haptic interactions with the finger or hand. Alternatively, the user can hold the device at a point behind to simulate the exploration of a virtual environment with the tip of a tool. The benefit of such a mechanical decoupling of the angular from the translational DOF is twofold. First, it results in reduced natural dynamics of the orientational DOF and second, the torque capability of the actuators can be chosen to match the capability of a human wrist. Coupled designs usually tend to an unnecessary large torque capability requiring additional safety measures.

The mechanical realisation of this kinematical design is without joint angle limits and possibility for collision between parts of the structure. One important goal pursued

TABLE I
LINK LENGTH DESIGN OF ViSHARD10

Link i	Length
$l_1 = l_2 = l_3 = l_4$	0.25 m
$l_{5h} = l_8$	0.47 m
l_{5v}	0.71 m
$l_6 = l_7$	0.212 m
l_9	0.15 m
l_{10}	0.15 m

TABLE II
TARGET SPECIFICATIONS OF ViSHARD10

Property	Value
workspace	cylinder $\varnothing 1.7 \text{ m} \times 0.6 \text{ m}$ 360° for each rotation
peak force	170 N
peak torque	pitch, yaw: 13 Nm roll: 4.8 Nm
translational velocity	> 1 m/s
maximum payload	7 kg
mass of moving parts	$\approx 23 \text{ kg}$

with the kinematical design of ViSHARD10 has been to provide the option to partition the inverse kinematics problem into two separate problems: the inverse kinematics for the positioning and the orientation stage. This can decrease the computational power required for the redundancy resolution significantly. The decoupling of the translational from the rotational movement is achieved when controlling joint 6 and 7 to mimic the operation of a prismatic joint. The distance between joint axis 10 and joint 9 is 0.1 m providing sufficient mounting room for end-effectors of moderate size. The link length design (see table I) gives an overall system size similar to ViSHARD6 (see figure 1). The dexterous workspace, however, which is a cylinder with $\varnothing 1.7 \text{ m} \times 0.6 \text{ m}$, is significantly larger.

The actuation torque is provided by DC-motors coupled with harmonic drive gears offering zero backlash. The moment stiffness of the gears in the SCARA segment is increased by additional bearing support in order to avoid damage due to deflection in the harmonic drive component sets. The motors and the gears have been selected to meet the target specifications summarised in Tab. II. In order to permit force feedback control the device is equipped with a six-axis JR3 force-torque sensor providing a bandwidth of 8 kHz at a comparatively low noise level. The joint angles are measured by digital MR-encoders with a resolution of 4096 counts per revolution, resulting in a comparatively high position resolution when multiplied with the gear ratio varying from 100:1 to 160:1.

D. Safety measures

For such a large interface with high output capability careful attention has to be paid to safety measures ensuring that a computer or device malfunction does not result in user injury. On this account appropriate safety mechanism have to be developed. An integrated circuit takes care of a

safe work with the haptic display. The operation principle is based on a watchdog and a shut-off mechanism depending on joint velocities. The watchdog ensures that the real-time process is running and signals are updated according to the implemented control strategies. In case of a computer crash the watchdog mechanism stops the application. To protect the operator against unpredictable very fast motions of the haptic display a shut-off mechanism depending on joint velocities is provided. Thereby a joint velocity threshold can be set by adjusting time unit and counting velocity of a so called reference counter. A second parallel working counter counts the occurring encoder impulses. If the counted encoder impulses exceed the counter reading of the reference counter the application stops immediately. Furthermore in case of emergency motors are bypassed and act as brakes. Finally several emergency stop buttons and a dead-man's button are provided (for bimanual operation the dead-man's button can be accomplished as foot-pedal).

IV. CONTROL OF ViSHARD10

A. General control scheme

The haptic simulation of a human's bilateral interaction with a virtual environment requires the control of the motion-force relation between operator and robot. This can be achieved by either controlling the interaction force of the device with the operator (impedance display mode) or the device motion (admittance display mode).

In the former approach, also called impedance display mode, the robot acts as impedance and the human as admittance. In other words the robot accepts the human's motion input and gives force output according to the impedance of the simulated environment. Impedance controlled devices do not necessarily require force measurement, frequently simple open loop force control schemes are used. Force feedback, however, reduces the disturbance forces due to the natural device dynamics significantly. Impedance control usually used for light and highly backdrivable devices provides good results in rendering low impedances. A drawback of these algorithms is that a dedicated shaping of the closed loop impedance error due to natural device dynamics is hard to obtain as it strongly relies on the accuracy of the dynamic model. For robots with considerable anisotropic dynamics the operator will usually get a somewhat peculiar impression at low impedance haptic display.

Admittance control is particularly well suited for robots with hard non-linearities and large dynamic properties compared to the virtual environment being emulated. In this display mode forces are measured and motion is commanded, i.e. the robot acts as admittance and the human as impedance. Accordingly, a force sensor is required for admittance control. The high gain inner control loop closed on motion allows for an effective elimination of nonlinear device dynamics as for instance friction. Contrary to haptic displays driven in the impedance mode it is thus possible to render an isotropic closed-loop dynamic behaviour in order to provide the operator a more "natural feeling". The

drawback is the reduced capability for the display of low impedances.

Since the specifications of ViSHARD10 in terms of workspace and force capacity pose limits to the reduction of the natural device dynamic properties an operation in the admittance display mode is preferred as illustrated in figure 6. The interaction force f_{ext} of the operator is measured by a force-torque sensor. The virtual environment, modelled as admittance, relates the measured force to the desired end-effector velocity \dot{x}_d . An algorithm for inverse kinematics resolution (see Sec. IV-B) calculates the desired joint velocities \dot{q}_d . The desired joint angles q_d are then the reference input to a conventional control law, e.g. a computed torque scheme [26].

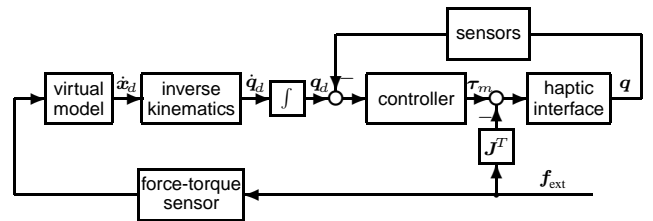


Fig. 6. Admittance control scheme

It has to be noted that the virtual environment does not necessarily need to be implemented as an admittance. A common variation to the scheme above is to compare the force output of a virtual impedance with the measured force and then to transform the error through an admittance into the desired velocity (position-based impedance control).

B. Inverse kinematics

The mapping

$$\dot{x}_E = J\dot{q} \quad (1)$$

relates the n -dimensional joint velocity vector \dot{q} to the m -dimensional end-effector velocity vector \dot{x}_E , where J is the $m \times n$ Jacobian matrix of the manipulator. If $n > m$ the manipulator is said to be redundant with respect to the end-effector task and $n-m$ DOF are available to solve the redundancy on the condition that J is full rank. In this case the range space of J is the entire \mathbb{R}^m and the $n-m$ dimensional null space is spanned by the last $n-m$ input vectors v_i of the matrix V , which can be found by the singular value decomposition

$$J = U\Sigma V^T, \quad (2)$$

where $\Sigma = [S \ 0]$ is the $m \times n$ matrix with S containing the singular values σ_i of J on its diagonal. As J approaches rank deficiency the singular value σ_m tends to zero and the end-effector velocity produced by a fixed joint velocity inline with v_m decreases. At singular configurations, i.e. $r = \text{rank}(J) \leq m$, joint velocities along the last $n-r$ input singular vectors v_i fall into the nullspace of J , meaning that no end-effector motion is achieved.

1) *Pseudoinverse control:*

As proposed by Whitney [27] redundancy resolution can be done, by finding joint velocities $\dot{\mathbf{q}}$ that minimise $\dot{\mathbf{q}}^T \dot{\mathbf{q}}$ subject to (1) using the Moore-Penrose generalized inverse $\mathbf{J}^\#$ of the Jacobian matrix, which yields

$$\dot{\mathbf{q}} = \mathbf{J}^\# \dot{\mathbf{x}}_E . \quad (3)$$

Although the motion is pointwise optimal in a least squares sense, meaning that the joint velocities are kept as small as possible, there is no guarantee that the manipulator avoids singular configurations. In order to solve this problem Liegeois [28] proposed the additional usage of the nullspace projection operator

$$\dot{\mathbf{q}} = \mathbf{J}^\# \dot{\mathbf{x}}_E + [\mathbf{I} - \mathbf{J}^\# \mathbf{J}] \dot{\mathbf{q}}_0 , \quad (4)$$

to project the joint velocities $\dot{\mathbf{q}}_0$, defined by a suitable choice of some side criterion, onto the nullspace of \mathbf{J} . The potential function $H(\mathbf{q})$ depending on the joint angles \mathbf{q} can be used as a side criterion, which has to be extremised using the gradient minimisation or maximisation of potential fields. Thus the joint velocities $\dot{\mathbf{q}}_0$ can be defined as

$$\dot{\mathbf{q}}_0 = \alpha \nabla H(\mathbf{q}) \quad (5)$$

A vast variety of such side criteria $H(\mathbf{q})$ has been proposed in the literature. Hooper *et al.* [29] list 30 criteria covering the evaluation of the manipulator inertial, geometric, compliance, and kinetic energy performance as well as the distance from physical constraints.

In order to avoid singular configurations often a potential function evaluating the manipulability of the device is applied. The term manipulability can be understood as a definition of how easily and uniformly the manipulator can move around the workspace. Yoshikawa [30] first introduced a quantitative measure of manipulability as

$$w = \sqrt{\det \mathbf{J} \mathbf{J}^T} = \sigma_1 \sigma_2 \dots \sigma_m , \quad (6)$$

where σ_i is a singular value obtained by the SVD (2) of \mathbf{J} ; w can be used as a potential function $H(\mathbf{q})$. Introducing normalised joint velocities

$$\hat{q}_i = \frac{\dot{q}_i}{\dot{q}_{i,\max}} \quad \text{such that} \quad \hat{\mathbf{q}}^T \hat{\mathbf{q}} \leq 1 , \quad (7)$$

one can get further insight into the shape of the subset \mathcal{S}_v of realizable end-effector velocities $\dot{\mathbf{x}}_E$. Using the normalised joint velocities, (1) can be rewritten as

$$\dot{\mathbf{x}}_E = \mathbf{J} \mathbf{W}_q^{-1} \hat{\mathbf{q}} , \quad (8)$$

where $\mathbf{W}_q = \text{diag}(1/q_{i,\max})$ is the $n \times n$ weighting matrix and $\hat{\mathbf{J}} = \mathbf{J} \mathbf{W}_q^{-1}$ the weighted Jacobian matrix. With the singular value decomposition of the weighted Jacobian according to (2) the $\|\cdot\|_2$ norm of $\hat{\mathbf{q}}$ follows as

$$\frac{\dot{x}_{E1}^2}{\sigma_1^2} + \dots + \frac{\dot{x}_{Em}^2}{\sigma_m^2} \leq 1 , \quad (9)$$

where $\dot{\mathbf{x}}_E = \mathbf{U}^T \dot{\mathbf{x}}_E$. As σ_1 is the maximum singular value, the maximum end-effector velocity $\dot{\mathbf{x}}_{E,\max} = \sigma_1$ is achieved

in the direction of the singular vector \mathbf{u}_1 considering that the joint-velocities satisfy $\|\hat{\mathbf{q}}\|_2 \leq 1$. Equation (9) is called the manipulability ellipsoid. The volume V_m of the manipulability ellipsoid is then given with

$$V_m(\mathbf{J}) = \frac{\pi^{\frac{m}{2}}}{\Gamma(1 + \frac{m}{2})} \prod_{i=1}^m \sigma_i , \quad (10)$$

where m is the dimension of the manipulability ellipsoid and $\Gamma(\cdot)$ the Gamma function. By comparison one can see that the manipulability measure defined in (6) provides a measure for the volume of the ellipsoid. The directional characteristics of the input-output transmissivity is, however, not evaluated. Another deficiency is that translational and rotational manipulabilities are not distinguishable. In order to overcome these deficiencies new manipulability measures have been suggested by Hong *et al.* [31]. Applying the well known condition number

$$\kappa(\mathbf{J}) = \frac{\sigma_{\max}}{\sigma_{\min}} \quad (11)$$

as a measure of the directional uniformity of $\hat{\mathbf{J}}$, they defined a new manipulability measure with

$$m = \frac{V_m(\hat{\mathbf{J}})}{\kappa(\hat{\mathbf{J}})} . \quad (12)$$

Partitioning of the weighted Jacobian $\hat{\mathbf{J}}$ into orientational and translational parts

$$\begin{pmatrix} \mathbf{v}_E \\ \boldsymbol{\omega}_E \end{pmatrix} = \begin{pmatrix} \hat{\mathbf{J}}_v \\ \hat{\mathbf{J}}_\omega \end{pmatrix} \hat{\mathbf{q}} , \quad (13)$$

they defined the translational and rotational manipulability measure to be

$$m_{\text{TVM}} = \frac{V_m(\hat{\mathbf{J}}_v)}{\kappa(\hat{\mathbf{J}}_v)} \quad \text{and} \quad m_{\text{RVM}} = \frac{V_m(\hat{\mathbf{J}}_\omega)}{\kappa(\hat{\mathbf{J}}_\omega)} , \quad (14)$$

respectively. Applying these measures as side criterion for (5), one aims at a simultaneous minimisation of the condition number κ and maximisation of the volume V_m of the ellipsoid.

The combination of multiple optimisation criteria is easily achieved by the formulation of one single composite performance index ψ as for example by using the weighted sum

$$\psi = w_1 C_1(\mathbf{q}) + w_2 C_2(\mathbf{q}) + \dots + w_n C_n(\mathbf{q}) , \quad (15)$$

where $w_i > 0$ are the weighting factors and C_i normalised criteria values.

Determining the joint velocities according to (4) physical limitations to the maximum joint rates have to be considered to ensure that the manipulator can follow the commanded trajectory. Equation (4) can be rewritten as

$$\dot{\mathbf{q}} = \dot{\mathbf{q}}_p + \alpha \dot{\mathbf{q}}_h \quad (16)$$

where $\dot{\mathbf{q}}_p$ is the minimum-norm solution and $\dot{\mathbf{q}}_h$ the homogeneous solution. Based on constraints on the joint rates a bound on the step length α can be determined [32].

With \dot{q}_{il} and \dot{q}_{iu} being the lower and upper bound on the velocity for joint i one can write

$$\alpha_{i,\min} = \min\{(\dot{q}_{iu} - \dot{q}_{ip})/\dot{q}_{ih}, (\dot{q}_{il} - \dot{q}_{ip})/\dot{q}_{ih}\} \quad (17)$$

$$\alpha_{i,\max} = \max\{(\dot{q}_{iu} - \dot{q}_{ip})/\dot{q}_{ih}, (\dot{q}_{il} - \dot{q}_{ip})/\dot{q}_{ih}\} \quad (18)$$

for $i = 1, \dots, n$. Thus, the lower and upper bounds on α ensuring admissible joint rates are given by

$$\alpha_{\min} = \max\{\alpha_{1,\min}, \alpha_{2,\min}, \dots, \alpha_{n,\min}\} \quad (19)$$

$$\alpha_{\max} = \min\{\alpha_{1,\max}, \alpha_{2,\max}, \dots, \alpha_{n,\max}\}. \quad (20)$$

2) Inverse function:

Another approach to solve the redundancy is to define a single inverse function giving the joint coordinates for each point in a specified subset of the end-effector space. In contrast to pseudoinverse control these algorithms are cyclic (every closed path in the end-effector space is tracked only by closed paths in the joint space) avoiding unpredictable joint motions. Whereas it is in general not possible to define such a single inverse function for the whole six DOF end-effector space no matter how much redundant joints are used (see [33] for a proof) this approach may be rewarding in case the application does not require such a large workspace.

A simple inverse function can be defined when controlling the SCARA segment and joint 6 and 7 to mimic the operation of three prismatic joints:

$$\theta_1 = \arccos \frac{y}{2l_1} - \frac{3}{2}\pi, \quad \theta_2 = -2 \arccos \frac{y}{2l_1} + 2\pi, \quad (21)$$

$$\theta_3 = \arccos \frac{x}{2l_3} - \theta_1 - \theta_2, \quad \theta_4 = -2 \arccos \frac{x}{2l_3} + 2\pi, \quad (22)$$

$$\theta_6 = \arccos \frac{z}{2l_6}, \quad \theta_7 = -2\theta_6, \quad (23)$$

where x, y, z is the end-effector position respective the coordinate system $\{B\}$ defined in Fig 4. Setting joint angle 5 to $\theta_5 = \theta_{5,0} - \sum_{i=1}^4 \theta_i$ a unique solution to the inverse kinematics problem can be determined. The choice for the constant $\theta_{5,0}$ affects the location of the interior singularity of the angular workspace.

3) Partitioned inverse kinematics solution:

A decoupling of the translational from the rotational movement of VISHARD10 can be achieved when controlling joint 6 and 7 to mimic the operation of a prismatic joint with $\theta_7 = -2\theta_6$. Then the inverse kinematics for these joint is given by (23), where z is the end-effector height. Defining \mathbf{q}_{xy} to be the vector of the first four joint angles, \mathbf{J}_{xy} the 2×4 submatrix of the manipulator Jacobian obtained by removing row 3 to 6 and column 5 to 10, and \mathbf{v}_{xy} the vector containing the end-effector position in the x - y -plane, the solution for the joint rates of joint 1 to 4 is

$$\dot{\mathbf{q}}_{xy} = \mathbf{J}_{xy}^\# \mathbf{v}_{xy} + [\mathbf{I} - \mathbf{J}_{xy}^\# \mathbf{J}_{xy}] \alpha_{xy} \nabla H_{xy} \mathbf{q}_{xy}. \quad (24)$$

By setting $\mathbf{q}_{\text{rot}}^T = [\theta_5^* \ \theta_8^* \ \theta_9 \ \theta_{10}]$ with $\theta_5^* = \theta_5 + \sum_{i=1}^4 \theta_i$ and $\theta_8^* = \theta_8 + \sum_{i=6}^7 \theta_i$ the inverse kinematics for $\dot{\mathbf{q}}_{\text{rot}}$ is decoupled from the translational movement:

$$\dot{\mathbf{q}}_{\text{rot}} = \mathbf{J}_{\text{rot}}^\# \boldsymbol{\omega} + [\mathbf{I} - \mathbf{J}_{\text{rot}}^\# \mathbf{J}_{\text{rot}}] \alpha_{\text{rot}} \nabla H_{\text{rot}} \mathbf{q}_{\text{rot}}. \quad (25)$$

Here $\boldsymbol{\omega}$ is the rotational Cartesian velocity command and $\mathbf{J}_{\text{rot}} \in \mathbb{R}^{3 \times 4}$ the Jacobian relating \mathbf{q}_{rot} to $\boldsymbol{\omega}$. This partitioned solution reduces the computation significantly.

V. VIRTUAL ENVIRONMENT

The construction of virtual environments for haptic applications is carried out in two steps, namely the visual and the haptic rendering. Once realised the graphic representation (visual rendering) it must be filled with physical "meaning" by haptic rendering. This section first deals with the basics of graphic programming, then a method for haptic rendering is explained considering a virtual wall as example and finally the concrete realisation of a more complex virtual scenario is introduced.

A. Visual rendering

Nowadays professional program libraries (e. g. OpenGL or DirectX) are available for modern graphic applications. The instruction set of these libraries allows programming and graphic rendering of 3D models. In a first step the graphic objects (shapes, texts or pictures) are generated. Then the context is established with the help of appropriate attributes which describe how the representation (rendering) of the graphic objects shall happen. At last the representation of these objects provided with context is triggered.

The basic concept of most graphic applications is the scene graph [34]. This data structure is a directed acyclic graph with one root node, see figure 7. All objects, qualities and dependences of the elements contained in a scene are described by this graph. Several of these scene graphs can be summarized in one scene database to complex virtual scenarios. The basic element of this database is the node. It describes the form of an object (e. g. sphere, cube, cylinder, etc.) or its attributes (e. g. colour, transformation, lights, etc.). A node can be part of a group, which combines further nodes. The qualities of a node or a group (e. g. translations) can be passed on to hierarchically subordinate nodes. The scene graph is rendered from above to below and from left to right. A node lying on the right inherits the qualities of the previous nodes. For the description of an object and its qualities the order of the nodes in a group is important. Nodes on the right take on the qualities of the nodes added before or overwrite these if they have the same type as the already inserted one. The object form describing node must be laid out as the latter after the qualities describing nodes.

B. Haptic rendering

Besides visual rendering, forces and torques caused in the virtual environment must be simulated. Haptic displays allow to touch, feel and manipulate virtual environments. As shown in [35] successful virtual environments must offer haptic primitives like springs, rubber bands, inertia, friction or non-linearities (virtual walls).

In order to provide haptic feedback in harmony with the virtual environment, collisions with virtual objects must be detected [36]. Some free software solutions are available (e.

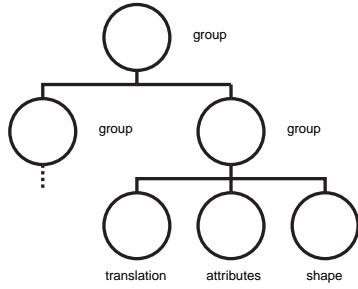


Fig. 7. Scene graph

g. SWIFT++, SOLID, VCollide). For simple configurations it is possible to determine the distance of two objects or the penetration depth in real time. However, problems occur in more complex scenarios, where multiple vertices of one object can collide simultaneously with the surface of a second object. As the collision detection and the haptic feedback uses discrete time steps, unrealistic oscillations might occur. Alternatively to the collision detection software, simple if-then-conditions are sufficient for simple scenarios. The nonlinear transition between free motion and contact with a solid wall is described like:

IF virtual wall THEN condition ELSE free motion

This condition causes a very sudden transition of the kinematic conditions. Therefore a wall can be used as a benchmark for performance comparisons between haptic interfaces. This method for construction of virtual environments reaches its limits at more complex objects since the programming effort rises excessively. But a virtual wall can be implemented easily using this simple condition. The practical realisation contains, however, some difficulties: Especially very stiff walls tend to vibration at the moment of contact. Non-passive behaviour of this kind doesn't match the experiences which an operator knows from real walls. This phenomenon called chatter depends on a various number of factors like haptic interface device properties, human's impedance, controller design, unmodelled system dynamics and/or sensor signal quantisation. Whereby some of these mechanism can be avoided by informed mechanical design, others are more difficult to avoid. The main problem presents the time-discrete realisation of the virtual wall [37] and the resultant energy losses arising due to delays (e.g. zero-order-hold operation) and asynchronous switching times (possible asynchrony of wall threshold crossings with sampling times) [38]: The reaction force f which counteracts the manipulator from the virtual wall is calculated to

$$f = k\Delta x + bv_x \quad (26)$$

with the stiffness k of the virtual wall the penetration depth x , the damping coefficient b , and the manipulator speed v_x . When driving into the wall the sampled manipulator position is closer to the wall surface than the manipulator itself and therefore f is calculated to low compared with a real wall. By contrast while moving out of the wall the

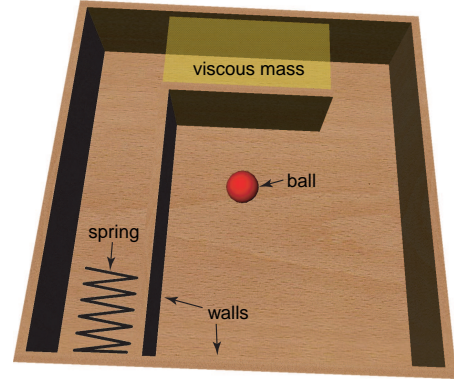


Fig. 8. Virtual labyrinth

sampled position is deeper inside the wall than the actual manipulator position and the force is calculated to high. The virtual wall becomes active and generates energy.

The mathematical description of the wall corresponds to the already introduced condition. Within the wall ($x < x_{wall}$) the reacting force is calculated to

$$f_{wall} = k_{wall}(x - x_{wall}) + b_{wall}v_x \quad (27)$$

with the wall stiffness k_{wall} and the damping coefficient b_{wall} . For free motion follows with the damping coefficient b_{free} and the manipulator speed:

$$f_{free} = b_{free}v_x. \quad (28)$$

As shown by [37] typical sampling rates for probing the condition $x < x_{wall}$ are about 300 to 1000Hz. Furthermore hysteresis can be introduced to dispel chatter and improve perceived hardness.

C. Implementation of a virtual labyrinth

For the implementation of the visualisation the open source library Open Inventor for Linux is used. A detailed introduction can be found in [39]. The controller is implemented in Matlab/ Simulink using Real-Time Workshop. The virtual scenario consists of stiff walls, a damping and a spring zone (see figure 8).

The resulting labyrinth gets combined of rectangles with predefined dimensions. Through this the corner coordinates can be used as well for building the visualisation as for the if-then statements of the haptic rendering. The visualisation requires only the actual position of the ball (hand position) transmitted. No feedback needs to be sent since the haptic rendering takes place inside the control loop. figure 9 shows a typical implementation of a virtual environment, modelled as admittance, which relates the measured force f to the desired end-effector position x . The forces measured by the force torque sensor f reduced by the reflection forces f_r are multiplied with the inverted mass matrix. The resulting positions x are transmitted to the visualisation and serve as desired values for the position control loop (see figure 6).

The haptic rendering of the virtual environment is calculated through the nonlinear function

$$f_r = \mathbf{K}(x)x + \mathbf{B}(x, \dot{x})\dot{x}. \quad (29)$$

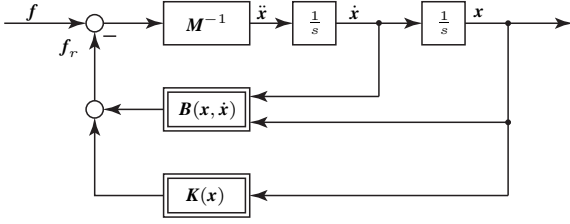


Fig. 9. Admittance implementation of a virtual environment

The ball is supervised for the collision detection. The spring force of the wall rises proportionally with the penetration depth. The damping is independent of the penetration depth, but it is, however, dependent on the movement direction of the ball. To avoid sticking when leaving the wall damping is only active if the speed of the ball is directed towards the wall. To find the appropriate stiffness of the wall we calculate the transfer function $F(s)$:

$$F(s) = \frac{1}{ms^2 + bs + k}. \quad (30)$$

The natural frequency ω_0 of the system is

$$\omega_0 = \sqrt{\frac{k}{m}} \quad (31)$$

and the global damping

$$d = \frac{b}{2m\sqrt{\frac{k}{m}}}. \quad (32)$$

With the optimal global damping $d_{opt} = \sqrt{2}/2 \approx 0.707$ we get the optimal stiffness

$$k_{opt} = \frac{b^2}{2m} \quad (33)$$

for shortest transient time and thereby little vibrations when touching the wall.

VI. NUMERICAL SIMULATION EXPERIMENTS

To compare the full with the partitioned inverse kinematics solution approach we carried out different numerical simulation experiments: We started with an evaluation of a set of inverse kinematics solution strategies. Based on the results of this evaluation we studied the device performance by means of manipulability for a couple of end-effector trajectories. Additionally we analysed the dependency on different end-effector heights and velocities.

For the evaluation we considered the following set of inverse kinematics solution strategies:

- nonopt: pseudoinverse control, see (3),
- man.: maximisation of the translational and rotational manipulability $V_m(\dot{\mathbf{J}}_v)$ and $V_m(\dot{\mathbf{J}}_\omega)$, see (10) and (13),
- dir. man.: maximisation of the translational and rotational manipulability considering the directional characteristics, see (14),
- cond.: minimisation of the translational and rotational condition number, see (11) and (13).

The translational and rotational performance indices have been combined to one optimisation criterion after (15). All these experiments have been conducted for the full and the partitioned inverse kinematics solution approach. A violation of joint velocity constraints has been avoided by keeping the step length α within the bounds given in (19) and (20).

It has to be noted that a comparison of the results has to be acted with caution since they are highly dependent on the choice of the step length α and the weighting factors w_i . For these experiments we normalised the performance indices by the average of the maximum performance value among a set of end-effector positions and orientations. Due to this normalisation we decided to weight the translational and rotational performance equal with $w_1 = w_2 = 1$. By experimentation we found that the normalisation also resulted for all side criteria in a similar maximum step length not producing selfmotion oscillations. Thus we set $\alpha = 1$ in these experiments. This procedure allows for a rough comparison of the different inverse kinematics solution approaches, minor deviations can, however, change when fine-tuning the normalisation, weighting factors, and step length.

The end-effector has been commanded to follow a circular trajectory in the x - y -plane at a velocity of 1 m/s with joint axis 1 at the center while keeping the orientation and height fixed. This procedure has been repeated for a set of radii r_i ranging from 0.05 m to 0.8 m. The initial end-effector position is given with $x_e = r_i$, $y_e = 0$ m, and $z_e = -0.36$ m respective the coordinate system $\{B\}$ defined in figure 4. The initial configuration of the joint angles is given with $[\theta_2 \ \theta_4 \ \theta_6 \ \theta_7 \ \theta_8 \ \theta_9 \ \theta_{10}] = [-\frac{\pi}{4} \ -\frac{\pi}{4} \ \frac{5\pi}{6} \ \frac{\pi}{3} \ \frac{\pi}{2} \ -\frac{3\pi}{4} \ 0]$. Setting the y -position of joint 3 positive (elbow-up configuration) the angles of joint 1 and 3 are well defined. The joint angle 5 is then determined by $\theta_5 = \frac{\pi}{2} - \sum_{i=1}^4 \theta_i$.

Figure 10 shows for the full inverse kinematics solution approach the progression of the rotational and translational manipulability indices when the end-effector follows the trajectory with radius 0.8 m. One can see that the nonoptimised solution technique drives the system in a rotational singularity whereas all side criteria can effectively prevent such configurations. It is also evident that optimisations subject to the manipulability considering directional characteristics and the conditioning number produce similar results. This observation goes along with the outcome of the other experiments confirming that these criteria are not directly opposed. Also a comparison of the performance regarding the condition number shows similar results for the three optimisation approaches.

The results for the partitioned solution technique given in figure 11 clearly reveal the decoupling of the translational from the rotational DOF; the rotational manipulability index of the nonoptimised solution is not changing as the commanded orientation of the end-effector is fixed; the rotational stage is decoupled from the selfmotion of the SCARA segment. Because the movement of joint 6 and 7 can also be used to change the position in the x - y -plane

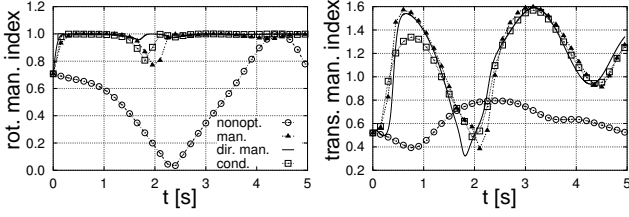


Fig. 10. Manipulability index at full inverse kinematics solutions for different inverse kinematic solution strategies; $r = 0.8$ m

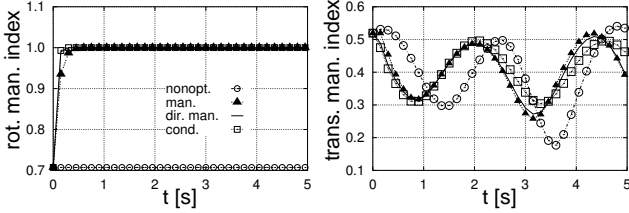


Fig. 11. Manipulability index at partitioned inverse kinematics solutions for different inverse kinematic solution strategies; $r = 0.8$ m

the translational manipulability index is affected by the orientation of joint 6 and 7. For the partitioned solution approach this orientation is not changed by the selfmotion of the translational stage. This explains the almost sinusoidal progression of the translational manipulability index. In the optimised solutions the orientation of joint 6 and 7 is changed by the selfmotion of the orientational stage during the first 0.3 seconds resulting in the "phase difference" when compared to the nonoptimised solution. It can also be seen that the optimisation prevents the SCARA segment to be driven in adversarial configurations as coming about at $t = 3.6$ s.

In figure 12 and 13 the device performance by means of manipulability is compared for trajectories with different radii. In all experiments the simulation has been stopped when the end-effector completed one circle except for the trajectory with $r = 0.05$ m. Since the end-effector velocity is set to 1 m/s just 0.31 seconds are required to complete one circle with $r = 0.05$ m. This is approximately the time period required for driving the device into a more dexterous configuration. Hence the simulation time has been extended to 1 s allowing for a more meaningful comparison of the optimised with the nonoptimised solution.

These results show that in case of the full inverse kinematics solution for all trajectories the rotational as well as the translational manipulability can be improved when applying additional side criteria. It is important to add that the nonoptimised solution drives the orientational stage to singular configurations for a radius of 0.4 m, 0.6 m, and 0.8 m. For the partitioned solution the improvement of the translational manipulability index is less significant. The reason for this is the decision to set the initial configuration of the SCARA segment close to optimum. Accordingly, the pseudoinverse solution produces results similar to the optimised solution. Needless to say that less dexterous initial configurations will give a larger benefit for the optimised solution.

The results also confirm that the interface can be op-

erated with the end-effector in regions close to the basis without significant impairment of the translational manipulability; the mean value is almost the same for trajectories with a radius of 0.05 m, 0.2 m, and 0.4 m. In no experiment the end-effector velocity of 1 m/s resulted in joint rates close to maximum.

Comparing the full solution with the partitioned solution in figures 12 and 13 exposes inferior results for the decoupled motion for this set of experiments. For a fair evaluation of these two approaches one has to consider that the difference in performance is highly dependent on the trajectory, the end-effector velocity and the initial manipulator configuration.

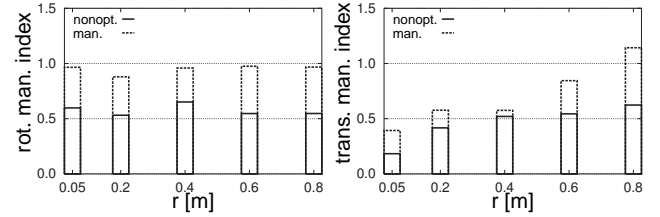


Fig. 12. Mean value of manipulability index at full inverse kinematics solution for a set of radii

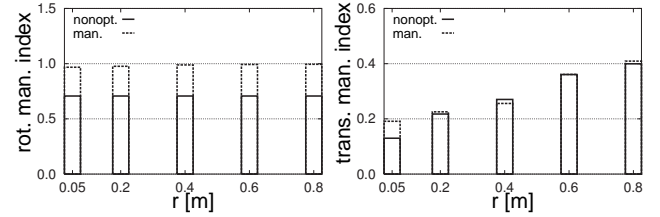


Fig. 13. Mean value of manipulability index at partitioned solution for a set of radii

To analyse the dependency on different end-effector heights z a circular trajectory has been repeated at the end-effector heights $z_1 = -0.3$ m, $z_2 = -0.15$ m, and $z_3 = 0$ m with $v = 1$ m/s (note that positive heights produce equal results due to symmetry).

The end-effector has been commanded to follow at constant velocity $v = 1$ m/s a circular trajectory with radius 0.4 m in the x - y -plane while keeping the height and orientation fixed. The initial end-effector position is given with $x = 0.8$ m, $y = 0$ m such that the end-effector is at the center of the x - y workspace when half of a circle is traversed (see Fig. 14). The initial configuration of the joint angles is given with $[\theta_2 \ \theta_4 \ \theta_9 \ \theta_{10}] = [0 \ 0 \ -\frac{3\pi}{4} \ 0]$. Setting joint angles 6, 7 according to (23), $\theta_5 = \frac{1}{2}\pi + \theta_1$, $\theta_8 = \theta_6$, and the y -position of joint 3 positive (elbow-up configuration) the angles of joint 1 and 3 are well defined.

By experiment we determined suitable weighting factors for the translational and rotational performance with $w_{\text{trans}} = 1$ and $w_{\text{rot}} = 2$. The maximum step length for the full solution not producing selfmotion oscillations has been found by experiment with $\alpha = 2.1$; for the partitioned solution we used $\alpha_{\text{trans}} = \alpha_{\text{rot}} = 0.53$.

The results for the optimised full inverse kinematics solution given in Fig. 15 shows that a largely increased translational dexterity for end-effector heights distant from

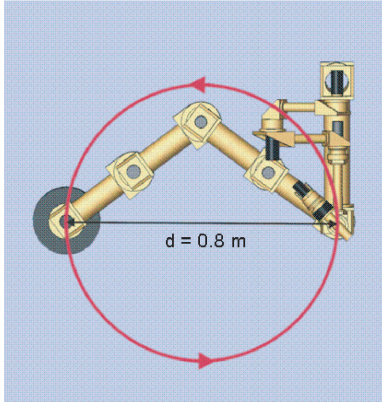


Fig. 14. Circular trajectory

$z=0$ m. The explanation is that the algorithm drives link 6 and 7 in an "outstretched" configuration (i.e. getting $|\theta_7|$ small). For initial configurations close to $z=0$ m the manipulator is trapped in a local minimum preventing this more dexterous "outstretched" configuration but resulting in a motion of joint 6, 7 similar to the partitioned solution. Consequently, a comparison of the full with the partitioned solution (see figure 16) gives at $z=0$ m an almost identical progression of the manipulability.

To interpret the translational manipulability results for the optimised partitioned solution (see figure 16) one has to consider that the selfmotion of the SCARA segment is decoupled from the end-effector height; the side criterion used for the optimisation of the null-space movement of the translational stage is based on J_{xy} only (dependent on joint angle 1 to 4). Thus, the motion of the SCARA joints is identical for all three trajectories (which also holds for the wrist joints). The translational manipulability index shown in figure 16 applies to the first three rows of J (dependent on joint angle 1 to 7).

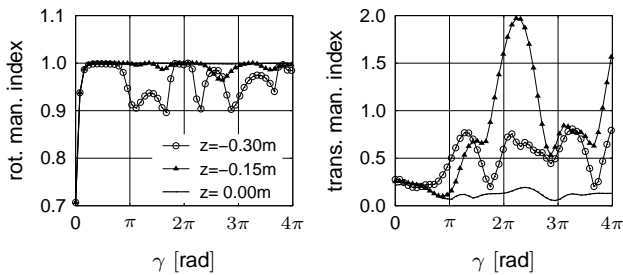


Fig. 15. Optimised full solution for different end-effector heights, $v=1$ m/s

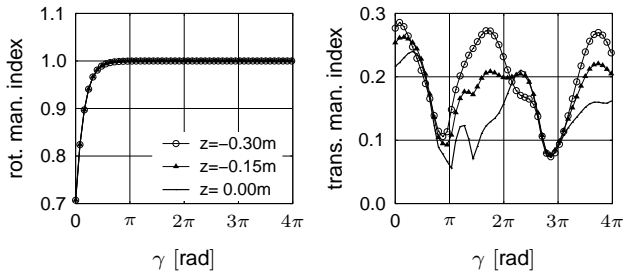


Fig. 16. Optimised partitioned solution for different end-effector heights, $v=1$ m/s

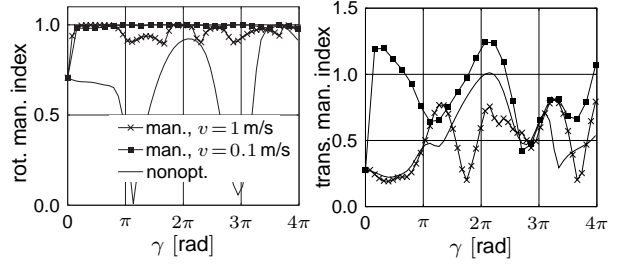


Fig. 17. Optimised full solution for different end-effector velocities, $z=0.3$ m

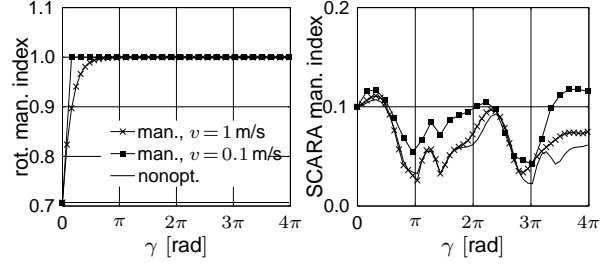


Fig. 18. Optimised partitioned solution for different end-effector velocities, $z=0.3$ m

Figure 17 and figure 18 show the progression of the manipulability indices when the end-effector follows the same circular trajectory at different velocities $v=0.1$ m/s and $\bar{v}=1$ m/s and an end-effector height $z=0.3$ m (the results for the nonoptimised solutions are independent of the velocity v). Please note, that the partitioned solution applies a manipulability index based on J_{xy} to optimise the SCARA selfmotion, see (24), whereas the index to evaluate the translational manipulability at the full solution applies to J_{xyz} , see (14).

The results for the *optimised full solution* show that the optimised device selfmotion can effectively prevent singular configurations. The progression of the translational manipulability at $v=1$ m/s illustrates that optimised Pseudoinverse control is a local inversion technique not necessarily giving results superior to the nonoptimised solution. The benefit of the optimisation is, however, more significant when v is decreased. Both observations also hold for the optimised partitioned solution.

A comparison of the results of the partitioned inverse solution with the full inverse solution technique exposes a significant potential for performance improvement when solving for all 10 DOF simultaneously. The reason is that in the full solution the movement of joint 6 and 7 is not only used to adjust the end-effector height but also to increase the workspace in the x - y -plane. Moreover, by driving link 6 and 7 in an "outstretched" configuration one can obviously increase the maximum velocity in height. It should be noted that such configurations result in an increase of motor torque required for the compensation of gravitational load. The main disadvantages of the full solution seem to be the increased computational effort and the coupling of the translational and rotational selfmotion. The coupled motion may be more difficult to understand and anticipate for the operator. As a consequence the full solution seems to be more likely to discomfort the user, which is subject to further investigations.

VII. CONCLUSIONS

In this paper we proposed the introduction of actuated kinematical redundancies in kinesthetic haptic hardware design to overcome performance limitations of non-redundant interfaces due to internal singularities. We presented the kinematical design of a highly versatile haptic interface VISHard10 with 10 actuated DOF offering a large workspace free of singularities and high force capability. The goal of this prototype is to provide a benchmarking testbed for the development and feasibility studies of novel haptic applications. We described the basic control strategy of the prototype along with inverse kinematics solution techniques. It turned out that the kinematical design allows for a decoupling of the translational from the rotational device movement enabling the partitioning of the inverse kinematics problem in two subproblems that can be solved separately to reduce computational effort. A comparison of this partitioned solution approach with the full solution reveals a significant potential for performance improvement when solving for all DOF simultaneously with the cost of increased joint velocities. The simulation results also show the benefit in terms of increased manipulability and effective singularity avoidance when applying techniques to optimise the device selfmotion. Furthermore we presented a construction possibility for virtual environments based on methods for visual and haptic rendering. Future work will include further in-depth studies of redundancy exploitation techniques specific to the goal of haptic human-device interaction, the implementation of dynamic model control algorithms, the implementation of tactile actuators, and the development of novel haptic applications e. g. dual handed open surgery.

ACKNOWLEDGEMENTS

This work is part of the TOUCH-HapSys project financially supported by the 5th Framework IST Programme of the European Union, action line IST-2002-6.1.1, contract number IST-2001-38040. For the content of this paper the authors are solely responsible for, it does not necessarily represent the opinion of the European Community.

REFERENCES

- [1] H. Esen, K. Yano, and M. Buss, "A control algorithm and preliminary user studies for a bone drilling medical training system," in *ROMAN*, 2003.
- [2] M. Buss and G. Schmidt, "Control Problems in Multi-Modal Telepresence Systems," in *Advances in Control: Highlights of the 5th European Control Conference ECC'99 in Karlsruhe, Germany*, P. Frank, Ed. Springer, 1999, pp. 65–101.
- [3] J. Brederson, M. Ikits, C. Johnson, and C. Hansen, "The visual haptic workbench," in *Proc. 5th PHANTOM Users Group Workshop*, 2000.
- [4] C. Richard, A. Okamura, and M. Cutkosky, "Getting a feel for dynamics: using haptic interface kits for teaching dynamics and control," in *ASME IMECE 6th Annu. Symp. on Haptic Interfaces*, Dallas, Texas, 1997.
- [5] Y. Nakamura, *Advanced Robotics: Redundancy and Optimization*. Addison-Wesley, 1991.
- [6] G. Hirzinger, N. Sporer, A. Albu-Schäffer, M. Hähle, R. Krenn, A. Pascucci, and M. Schedl, "DLR's torque-controlled light weight robot iii - are we reaching the technological limits now?" in *Proc. IEEE Int. Conf. Rob. Automat.*, 2002, pp. 1710–1716.
- [7] M. Ueberle and M. Buss, "Design, control, and evaluation of a new 6 DOF haptic device," in *Proc. IEEE/RSJ Int. Conf. on Intellig. Rob. and Syst.*, 2002, pp. 2949–2954.
- [8] J. Colgate and J. Brown, "Factors affecting the Z-width of a haptic display," in *Proceedings of the IEEE International Conference on Robotics and Automation*, 1994, pp. 3205–3210.
- [9] S. Eppinger and W. Seering, "Understanding bandwidth limitations in robot force control," in *Proceedings of the IEEE International Conference on Robotics and Automation*, 1987, pp. 904–909.
- [10] V. Hayward, "Toward a seven axis haptic device," in *Proceedings of the IEEE/RSJ International Conference on Intelligent Robotics and Systems*, 1995, pp. 133–139.
- [11] D. Lawrence and J. Chapel, "Performance trade-offs for hand controller design," in *Proceedings of the IEEE International Conference on Robotics and Automation*, 1994, pp. 3211–3216.
- [12] M. Girone, G. Burdea, and M. Bouzit, "The "Rutgers ankle" orthopedic rehabilitation interface," in *Proceedings of the ASME Haptics Symposium*, vol. 67, 1999, pp. 305–312.
- [13] T. Massie and J. Salisbury, "The PHANTOM haptic interface: A device for probing virtual objects," in *Proceedings ASME Winter Annu. Meeting: Dyn. Syst. and Contr.*, vol. 55, 1994, pp. 295–301.
- [14] V. Hayward, P. Gregorio, S. Greenish, M. Doyon, L. Lessard, J. McDougall, I. Sinclair, S. Boelen, X. Chen, J.-P. Demers, and J. Poulin, "Freedom-7: A high fidelity seven axis haptic device with application to surgical training," in *Experimental Robotics V*, ser. Lecture Notes in Control and Information Sciences 232, A. Casals and A. de Almeida, Eds. Springer-Verlag, 1998, pp. 445–456.
- [15] H. Esen, K. Yano, and M. Buss, "A control algorithm and preliminary user studies for a bone drilling medical training system," in *IEEE Int. Workshop on Robot and Human Interactive Communication*, Millbrae, CA, 2003, pp. 904–909.
- [16] G. S., F. Conti, P. Rouiller, P. Helmer, and C. Baur, "Overview of the Delta Haptic Device," in *Eurohaptics*, 2001.
- [17] C. Clover, G. Luecke, J. Troy, and W. McNeely, "Dynamic simulation of virtual mechanisms with haptic feedback using industrial robotics equipment," in *Proceedings of the 1997 IEEE International Conference on Robotics & Automation*, 1997, pp. 724–730.
- [18] J. Hoogen, R. Riener, and G. Schmidt, "Control aspects of a robotic haptic display for kinesthetic knee joint simulation," in *IFAC J. on Control Eng. Practice*, vol. 10, no. 11, 2002, pp. 1301–1308.
- [19] R. Adams, M. Moreyra, and B. Hannaford, "Excalibur - a three axis force display," in *Proceedings ASME Int. Mech. Eng. Congr. Exhib.*, 1999.
- [20] R. Van der Linde, P. Lammertse, E. Frederiksen, and B. Ruiters, "The HapticMaster, a new high-performance haptic interface," in *Eurohaptics'02*, 2002, pp. 1–5.
- [21] J. Hollerbach, "Optimum kinematic design for a seven degree of freedom manipulator," in *2nd International Symposium of Robotics Research*, 1984, pp. 215–222.
- [22] K. Kreutz-Delgado, M. Long, and H. Seraji, "Kinematic analysis of 7 dof anthropomorphic arms," in *Proceedings of the 1990 IEEE International Conference on Robotics & Automation*, 1990, pp. 824–830.
- [23] R. Williams II, "Local performance optimization for a class of redundant eight-degree-of-freedom manipulators," in *Proceedings of the 1994 IEEE International Conference on Robotics & Automation*, 1994, pp. 992–997.
- [24] F. Duarte, J. Machado, and L. Horváth, "A trajectory planning algorithm for redundant manipulators," in *Proc. IEEE Int. Symp. Ind. Electr.*, 1999, pp. 1002–1007.
- [25] G. Long, R. Paul, and W. Fisher, "The Hamilton wrist: a four-revolute-joint spherical wrist without singularities," in *Proceedings of the 1989 IEEE International Conference on Robotics & Automation*, 1989, pp. 902–907.
- [26] P. Khosla and T. Kanade, "Real-time implementation of the computed-torque scheme," *IEEE Trans. Rob. Automat.*, vol. 5, no. 2, pp. 245–253, 1989.
- [27] D. E. Whitney, "Resolved motion rate control of manipulators and human prostheses," *IEEE Transactions on Man-Machine Systems*, vol. MMS-10, pp. 47–53, 1969.
- [28] A. Liégeois, "Automatic supervisory control of the configuration and behaviour of multibody mechanisms," *IEEE Tans. on Syst., Man, and Cybern.*, vol. 7, no. 12, pp. 868–871, 1977.
- [29] R. Hooper and D. Tesar, "Motion coordination based on multiple performance criteria with a hyper-redundant serial robot example," in *Proceedings of the 1995 IEEE International Symposium on Intelligent Control*, 1995, pp. 133–138.
- [30] T. Yoshikawa, "Manipulability of robotic mechanism," *The Int. J. of Robotics Research*, vol. 4, no. 5, pp. 3–9, Summer 1985.

- [31] K.-S. Hong and J.-G. Kim, "Manipulability analysis of a parallel machine tool: Application to optimal link length design," *Journal of robotic Systems*, vol. 17, no. 8, pp. 403–415, 2000.
- [32] L. Li, W. Gruver, Q. Zhang, and Z. Yang, "Kinematic control of redundant robots and the motion optimizability measure," *IEEE Transactions on Systems, Man, and Cybernetics*, vol. 31, no. 1, pp. 155–160, 2001.
- [33] D. Gottlieb, "Topology and robots," in *Proc. IEEE Int. Conf. Rob. Automat.*, 1986, pp. 1689–1691.
- [34] A. Bentele, "Objektorientierte 3d-programmierung mit open inventor," *Seminar "Modelling and Rendering"*, 2002.
- [35] J. M. Brown and J. E. Colgate, "Physics-based approach to haptic display," in *Proceedings of the International Symposium on Measurement and Control in Robotics, Topical Workshop on Virtual Reality*, Houston, TX, 1994, pp. 101–106.
- [36] J. Mezger, S. Kimmerle, and O. Etmu, "Hierarchical techniques in collision detection for cloth animation," *Journal of WSCG*, vol. 11, no. 2, pp. 322–329, 2003.
- [37] R. B. Gillespie, "Haptic display of systems with changing kinematic constraints: The virtual piano action," Center For Computer Research in Music and Acoustics, Department of Music, Stanford, California, Tech. Rep. Report No. STAN-M-92, 1996.
- [38] R. B. Gillespie and M. R. Cutkosky, "Stable user-specific haptic rendering of the virtual wall," in *Proceedings of the International Mechanical Engineering Congress and Exhibition*, vol. 58, Atlanta, GA, 1996, pp. 397–406.
- [39] J. Wernecke, *The Inventor Mentor: Programming Object-Oriented 3D Graphics with Open Inventor*. Addison-Wesley Publishing Company, 1994.